

Vortex core dynamics and singularity formations in incompressible Richtmyer-Meshkov instability

Chihiro Matsuoka¹¹*Department of Physics, Ehime University, 2-5, Bunkyocho, Matsuyama, Ehime 790-8577, Japan*Katsunobu Nishihara²²*Institute of Laser Engineering, Osaka University, 2-6, Yamada-oka Suita, Osaka 565-0871, Japan*

(Received 13 May 2005; published 6 February 2006)

Motion of a fluid interface in Richtmyer-Meshkov instability is examined as a vortex sheet with the use of Birkhoff-Rott equation. This equation coupled with an evolution equation of the strength of the vortex sheet can describe all inviscid and incompressible fluid instabilities, i.e., Kelvin-Helmholtz, Rayleigh-Taylor, and Richtmyer-Meshkov instabilities, when Atwood numbers and initial distribution of vorticities are given. With these equations, detailed motion of a vortex core in the Richtmyer-Meshkov instability is investigated. For the Kelvin-Helmholtz and Rayleigh-Taylor instabilities, it is known that the curvature of a vortex sheet diverges at a finite time $t=t_c$. This fact indicates that the solution loses its analyticity at t_c . We show that the singularity formation also occurs in the Richtmyer-Meshkov instability and at the same time, accumulation of vorticity to some points where singularities are formed develops to the roll-up of a sheet when the sheet is regularized. We investigate motion of these accumulation points, i.e., vortex cores, and present that their trajectories and the strengths depend on the Atwood numbers.

DOI: [10.1103/PhysRevE.73.026304](https://doi.org/10.1103/PhysRevE.73.026304)

PACS number(s): 47.32.C-, 47.20.Ma, 02.70.Pt, 47.11.-j

I. INTRODUCTION

When a planar shock wave collides with a corrugated interface between two different fluids, a perturbed shock wave is transmitted and either a perturbed shock wave or a perturbed centered rarefaction wave is reflected. The perturbed wave fronts propagate the initial disturbance into the bulk of the fluids. As the shock (or rarefaction) fronts separate away, the perturbed interface begins to grow [1–5]. If the initial corrugation is very small compared with the perturbation wavelength, an asymptotic velocity is achieved when the fronts are sufficiently far from the initial contact discontinuity. This phenomenon, known as Richtmyer-Meshkov (RM) instability, is important in astrophysics, inertial confinement fusion, and supersonic combustion.

Refraction of flow across the perturbed wave fronts deposits localized nonuniform vorticity at the interface, which drives the RM instability [6–8]. The two distinct contributions to the linear asymptotic growth rate are separated in the following exact formula:

$$v_{\text{lin}} = \frac{\rho_1^* \delta v_1^* - \rho_2^* \delta v_2^*}{\rho_1^* + \rho_2^*} - \frac{\rho_1^* F_{s1}^* - \rho_2^* F_{s2}^*}{\rho_1^* + \rho_2^*} \equiv v_0 + \Delta v_s, \quad (1)$$

driven by Wouchuk and Nishihara (WN) [6]. Here $\rho_{1,2}^*$ and $\delta v_{1,2}^*$ are densities and transverse velocities immediately after the shock-interface interaction, suffixes 1 and 2 denote two different fluids, where the incident shock propagates through from fluid 1 to fluid 2, and $F_{s1,2}^*$ are parameters accounting the amount of vorticity left by the fronts in the bulk of the fluids. The first term is due to the instantaneous deposition of the localized vorticity at the interface just after the shock-interface interaction. The second term is determined from the sonic interaction between the interface and the fronts [7].

The WN formula of the asymptotic linear growth is valid for any value of the initial parameters, incident shock Mach number, fluid density ratio, and compressibility. Reference [6] also showed that the pressure and density perturbations between the fronts vanish when the fronts are sufficiently far away, independent of the incident shock strength. This means that the perturbed velocity field asymptotically becomes incompressible. Therefore, we have an asymptotic velocity shear of $v_{\text{lin}} - (-v_{\text{lin}})$ across the interface within the linear theory. It should be noted that the vorticity deposited at the interface is proportional to the product of the wave number and the preshocked corrugation amplitude for a single-mode sinusoidal corrugation in the small amplitude theory [6].

As discussed by Velikovich *et al.* [8], a large family of so-called RM-like interface instabilities exists, which is driven by the same physical mechanisms as the classical RM instability, namely by the nonuniform vorticity, either initially deposited at the interface or supplied from external sources. For instance, in the experiments reported by Jacobs *et al.* [9], the sinusoidal vorticity at an interface with a standing wave form separating two immiscible fluids contained in a tank grows due to the “virtual gravity” when the tank is in contact with a coil spring for a brief interval of time, but finite time [10]. In the linear theory, the vorticity deposited at the interface is also proportional to the product of the wave number and the preaccelerated corrugation amplitude [6,10]. The main features of the RM and RM-like instabilities at the linear regime are firmly established.

However, analytical treatments are still limited to such as a weakly nonlinear analysis performed in Refs. [11,12] only giving a short time behavior of the interface evolution, and a local expansion of Layzer type [13–16] or a nonlocal expansion theory with a multiharmonic analysis [17] only giving an asymptotic behavior of a bubble. Therefore, we need an-

other approach so as to describe throughout the interface dynamics from the linear regime to a fully nonlinear stage.

In the fully nonlinear stage of the RM instability, the spike rolls up to a spiral, as observed in Ref. [9], due to the non-uniform vorticity distributed at the interface initially. This work aims at presenting a long-time behavior of the interface dynamics, especially such as vortex core dynamics, that determines the spiral structure of the RM spike observed in Ref. [9], singularity formations at the interface and their dependence on the density ratio, in the two-dimensional incompressible RM instability by treating the interface as a vortex sheet. We distribute the initial vorticity at the interface given by the asymptotic linear theory for a single-mode sine corrugation. It should be mentioned that the asymptotic velocity is consistent with the previous compressible evolution of the perturbation within the linear theory. As will be introduced below, we use a normalized time as $kv_{\text{lin}}t$, where k is the wave number of the single mode. Therefore real time can be calculated from the knowledge of such as incident shock Mach number and fluid density ratio.

In order to investigate the vortex sheet motion stated above, we use the Birkhoff-Rott equation. The Birkhoff-Rott equation is known as an integro-differential equation that describes a vortex sheet motion in an inviscid and incompressible fluid [18–20]. It is usually used for calculations of a vortex sheet motion in a homogeneous fluid, where the circulation of a system is conserved according to Kelvin's theorem. The Birkhoff-Rott equation can be applied to an inhomogeneous fluid system with two different fluid densities, which we will consider here, providing an evolution equation of the circulation or strength of a vortex sheet. In the present work we examine an interface motion in the RM instability using the Birkhoff-Rott equation coupled with an evolution equation of the vortex strength at the sheet, which was first derived by Baker *et al.* [21] from the Bernoulli equation. The coupled equations describe all inviscid and incompressible instabilities of a fluid interface such as the Kelvin-Helmholtz (KH), Rayleigh-Taylor (RT), and RM instabilities. In this paper we classify these instabilities by the initial distribution of the vorticity and the linear growth rate as follows:

(i) There exists a uniform shear flow initially between two fluids in the KH instability, in which a linear mode grows exponentially and the exponent is proportional to the wave number k .

(ii) There exists no shear flow initially between two fluids in the RT instability, in which a linear mode grows exponentially and the exponent is proportional to \sqrt{k} .

(iii) There exists a nonuniform shear flow between two fluids in the RM instability, in which a linear mode grows proportional to time t , i.e., kt .

When we calculate the Birkhoff-Rott equation numerically, two methods are adopted in this study. One is the vortex method and the other is a quadrature method presented by Sidi and Israeli [22] for solving periodic singular integral equations of Fredholm type. It is mathematically proven that initial value problems to the Birkhoff-Rott equation are ill-posed in a certain nonanalytic function space and the solution loses its smoothness at a finite time [24], which indicates that the roll-up of a vortex sheet does not arise in the limit

that the system is inviscid and incompressible and the thickness of a vortex sheet is zero. However, a vortex sheet rolls up smoothly in real systems due to the existence of viscosity or finite thickness of the sheet. The vortex method is a method which regularizes the Cauchy integral of the Birkhoff-Rott equation with a small parameter δ introduced by Krasny [23]. This is an artificial parameter in order to calculate motion of a vortex sheet numerically for a long time. When $\delta \neq 0$, governing equations are not identical to the Euler equations. Here, we use this method in order to calculate the roll-up of an interface. The other method, the quadrature method presented by Sidi and Israeli [22] makes it possible to calculate the Cauchy integral with the exponential accuracy even if the regularized parameter $\delta=0$. By using the quadrature method for calculating Fourier amplitudes of the interface perturbation, we will examine whether the formation of the curvature singularity [26,27] occurs or not in the RM instability.

Some studies with the use of the Birkhoff-Rott equation are known for the RT and RM instabilities. Baker *et al.* [28] investigated the singularity formation in the limit of $\delta=0$ in the RT instability and presented a theoretical prediction that the singularity formation can occur in the RT instability excluding the case for $A=1$. Tanveer [34] also obtained the same results as Baker *et al.* independently with another approach. These studies for the singularity formations concerned whether or not the solution loses its analyticity in a finite time as found in the KH instability.

The formation of the curvature singularity has been believed to precede the roll-up of the vortex sheet when $\delta \neq 0$. The calculations by Kerr [29] for $\delta \neq 0$ guarantee this prediction. Kerr succeeded in long-time computations for the RT instability and showed roll-ups of the interface in the RT instability for various density ratios by using the semi-Lagrangian scheme with the second order Runge-Kutta method for the temporal integration. Kerr also investigated the asymptotic velocities of a bubble and spike in the RT instability and showed that they depend on the density ratio and are independent of the size of the regularized parameter δ . Kotelnikov *et al.* [30] reproduced a multimode profile in addition to a single mode perturbation in the RM instability experimentally observed by Jacobs *et al.* [31]. Sohn [32] applied the Godunov method to compute a nonlinear term in the evolution equation of the sheet strength and succeeded in long-time computations for both the RT and RM instabilities.

In this paper we perform more accurate computations than those described above and show the singularity formation in the RM instability in addition to the investigation of vortex core dynamics. We adapted other methods [25] besides the vortex method to study the roll-up of the vortex sheets. For those and their validness, refer to Ref. [25]. In Sec. II, we present kinematical and dynamical equations used for our numerical calculations. In Sec. III, detailed motion of a spiral core at which the strength of a vortex sheet becomes maximum in its absolute value is studied. In Sec. IV, we show the singularity formation in the RM instability, and in Sec V the counterparts in the RT instability are reviewed. Section VI gives conclusions and discussions.

II. GOVERNING EQUATIONS

We consider two incompressible fluids with different densities ρ_1 and ρ_2 . The Bernoulli equation, i.e., the pressure continuous condition at the interface in this system is given by [21]

$$\frac{d\Gamma}{dt} = -2A \frac{d\Phi}{dt} + A\mathbf{q} \cdot \mathbf{q} - \frac{A-2\alpha}{4} \boldsymbol{\kappa} \cdot \boldsymbol{\kappa} + \alpha A \boldsymbol{\kappa} \cdot \mathbf{q}, \quad (2)$$

where $A=(\rho_2-\rho_1)/(\rho_1+\rho_2)$ is the Atwood number, $\mathbf{q}=(\mathbf{u}_1+\mathbf{u}_2)/2$ is an average of the velocities on two sides with the velocity \mathbf{u}_i ($i=1,2$) in each side, $\Gamma=\phi_2-\phi_1$ is the circulation, ϕ_i ($i=1,2$) is the velocity potential in each side, $\Phi=(\phi_1+\phi_2)/2$ is the average velocity potential related with $\mathbf{u}_i = \nabla\phi_i$ and $\boldsymbol{\kappa}=\mathbf{u}_2-\mathbf{u}_1$ is the velocity difference between the boundary.

The system is supposed to be incompressible, therefore, the velocity potential satisfies the Laplace equation $\Delta\phi_i=0$ ($i=1,2$) in each region. The differentiation d/dt in Eq. (2) following a fluid particle on the interface with the velocity $\bar{\mathbf{u}}$ is defined to be

$$\frac{d}{dt} = \frac{\partial}{\partial t} + \bar{\mathbf{u}} \cdot \nabla, \quad \bar{\mathbf{u}} \equiv \mathbf{q} + \frac{\alpha \boldsymbol{\kappa}}{2},$$

where $|\alpha| \leq 1$ is a weighting factor such that $\alpha \neq 0$ when the Atwood number $A \neq 0$ [21]. Any values of the factor α satisfy the continuity condition of the normal velocity at the interface, however, we must carefully choose it when we perform numerical computations, in which smaller α enables us to calculate for a long time [33]. In computations for the roll-ups, $\alpha=-|A|^2$ is chosen for small Atwood numbers, while other values are taken for larger Atwood numbers following studies by Kerr [29]. When we examine singularity formations, we choose $\alpha=-A$ such that we can compare the theoretical work by Baker *et al.* [28]. It should also be noted that in the case of $\alpha=-A$, the velocity $\bar{\mathbf{u}}$ corresponds to the mass averaged interface velocity as used in our previous weakly nonlinear theory [12].

We consider an interface in the RM instability as a vortex sheet and suppose that the vortex sheet is described by $(x(t), y(t))$, where $x=X(\theta, t)$ and $y=Y(\theta, t)$, and θ is a La-

TABLE I. Simulation parameters; left, regularized vortex sheet ($\delta \neq 0$) and right, nonregularized vortex sheet ($\delta=0$).

	Regularized sheet (Secs. III and V A)	Nonregularized sheet (Secs. IV and V B)
N	512	1024
δ	0.15 (except Fig. 2)	0
α	$- A ^2$ ($A=0.155$), -0.05 (others)	$-A$
a_0	0.2	0.2
Fourier filter levels	10^{-13}	10^{-11}
Tolerance levels	10^{-8}	10^{-13}
Grid redistribution	used (except $A=0$)	Not used

grangian parameter which parametrizes the interface. Here, the system is assumed to be periodic in the x direction. The vortex strength $\kappa(\theta, t)$ is related to the circulation $\Gamma(\theta, t)$ through the relation $\kappa = \partial\Gamma/\partial s = \Gamma_\theta/s_\theta$, where the subscript denotes the differentiation with respect to the variable and s is arc length of the sheet. The vortex strength κ is also related with the velocity difference $\boldsymbol{\kappa}$ as $\boldsymbol{\kappa}t = \boldsymbol{\kappa}$, where $\mathbf{t} = (X_\theta, Y_\theta)/\sqrt{X_\theta^2 + Y_\theta^2}$ is a unit tangential vector of the interface. Then the Birkhoff-Rott equation that describes the motion of the vortex sheet in this system is given here as

$$\frac{\partial Z^*(\theta, t)}{\partial t} = \frac{1}{2\pi i} \text{PV} \int \frac{\kappa(\theta', t) s_\theta(\theta') d\theta'}{Z(\theta, t) - Z'(\theta', t)} + \frac{\alpha \kappa(\theta, t) Z_\theta^*(\theta, t)}{2s_\theta(\theta)}, \quad (3)$$

where the integral is Cauchy's principal value integral, $Z(\theta, t) = x + iy$, and Z^* is the complex conjugate of Z . This equation corresponds to the kinematic boundary condition in the system, and it describes the temporal evolution of the interface coupled with Eq. (2). Assuming the periodicity of the vortex sheet and separating the real and the imaginary parts in Eq. (3), we obtain

$$X_t = U + \frac{\alpha X_\theta}{2s_\theta} \kappa, \quad Y_t = V + \frac{\alpha Y_\theta}{2s_\theta} \kappa, \quad (4)$$

where $U=U(\theta, t)$ and $V=V(\theta, t)$ are given as

$$U(\theta, t) = -\frac{1}{4\pi} \int_{-\pi}^{\pi} \frac{\sinh(Y(\theta, t) - Y(\theta', t)) \kappa(\theta', t) s_\theta(\theta') d\theta'}{\cosh(Y(\theta, t) - Y(\theta', t)) - \cos(X(\theta, t) - X(\theta', t)) + \delta^2},$$

$$V(\theta, t) = \frac{1}{4\pi} \int_{-\pi}^{\pi} \frac{\sin(X(\theta, t) - X(\theta', t)) \kappa(\theta', t) s_\theta(\theta') d\theta'}{\cosh(Y(\theta, t) - Y(\theta', t)) - \cos(X(\theta, t) - X(\theta', t)) + \delta^2}. \quad (5)$$

We used here Krasny's δ [23] in order to regularize the singular integral in Eq. (3). These regularized equations (5) converge uniformly to the Birkhoff-Rott equation as $\delta \rightarrow 0$,

as long as the solution is smooth [35]. We set $\delta=0$ in Secs. IV and V B for calculating the singularity formation. For the validity of Krasny's δ , refer to Refs. [36–38]. Differentiating

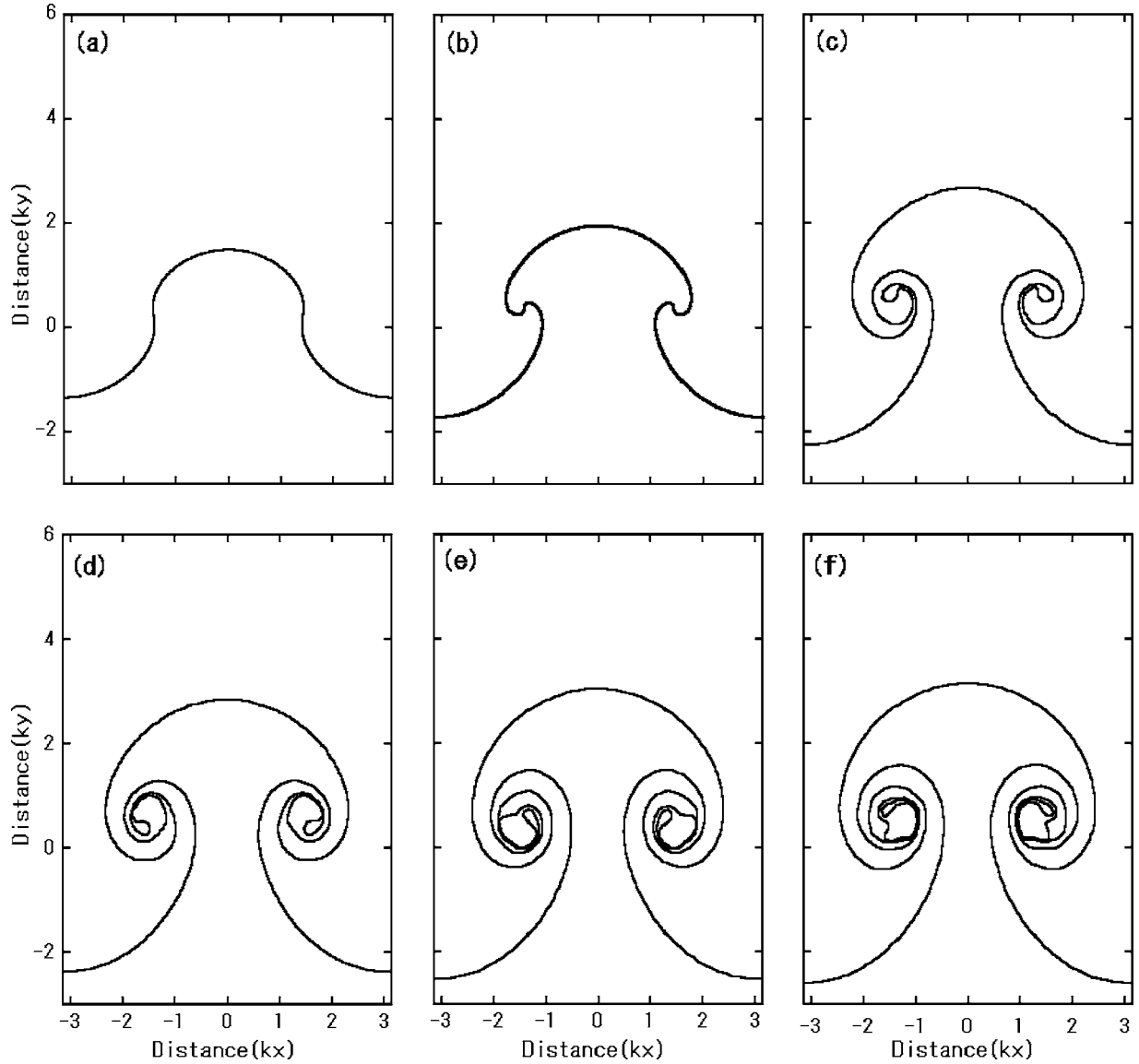


FIG. 1. Interfacial profiles in the RM instability for $A=0.155$ at dimensionless time $t =$ (a) 2.0, (b) 4.3, (c) 6.2, (d) 7.2, (e) 8.6, and (f) 9.4, where the initial configuration is given by Eq. (7).

Eq. (2) with respect to θ gives the following Fredholm integral equation of the second kind:

$$\begin{aligned} \kappa_t = & -\frac{2A}{s_\theta}(X_\theta U_t + Y_\theta V_t) - \frac{(1 - \alpha A)\kappa}{s_\theta^2}(X_\theta U_\theta + Y_\theta V_\theta) \\ & - \frac{A - \alpha}{4s_\theta}(\kappa^2)_\theta. \end{aligned} \quad (6)$$

By solving Eq. (4) coupled with Eq. (6), we can determine the temporal evolution of an interface as a vortex sheet in the RM instability.

Details of the numerical methods to solve Eqs. (4) and (6) are presented in the Appendix. For the temporal integration, we use the fourth-order Runge-Kutta scheme throughout this paper. The Fredholm equation of the second kind, Eq. (6) is solved by iteration until convergence within some tolerances (see Table I). In order to cut the irregular motion due to the

round-off error that increases with the number of vortex points N , we use the filtering technique introduced by Krasny [41]. The filter level depends on the spatial resolution, i.e., the number of grid points N and in general, the higher filter levels are demanded for the larger N . Details for numerical parameters presented in the following sections are summarized in Table I.

III. MOTION OF A SPIRAL CORE IN RICHTMYER-MESHKOV INSTABILITY

In this and the next sections for the RM instability, we normalize $X \rightarrow kX$, $Y \rightarrow kY$, $\theta \rightarrow k\theta$ ($-\pi \leq \theta \leq \pi$) and time $t \rightarrow kv_{lin}t$, where k is the wave number and v_{lin} is the linear growth rate in the system that is also related to the initial amplitude of the velocity potential $|\phi_1(0)| = |\phi_2(0)| = v_{lin}/k$ [12]. The initial amplitude of the sheet strength $\kappa(\theta, 0)$ is

also normalized by v_{lin} through the relations $\Gamma = \phi_2 - \phi_1$ and $\partial\Gamma/\partial s$.

We set here initial configurations of the interfacial profile $Z(\theta, 0)$ and the sheet strength $\kappa(\theta, 0)$ as

$$Z(\theta, 0) = \theta + ia_0 \cos \theta, \quad \kappa(\theta, 0) = -2 \sin \theta / s_\theta(0), \quad (7)$$

where the dimensionless initial amplitude a_0 is set to $a_0 = 0.2$. Roughly speaking, this normalized amplitude corresponds to the amplitude when the tank was separated from the coil spring in Jacobs's experiment [9], which is 0.3 cm in real scale [10]. We can also estimate $k = 0.81 \text{ cm}^{-1}$ and $kv_{\text{lin}} = 15.8 \text{ s}^{-1}$ in the linear theory [10], which leads to that normalized time $t = 1$ corresponds to real time 63.3 ms.

Figure 1 shows the temporal evolution of an interface for $A = 0.155$ over normalized time $0 \leq t \leq 9.4$, which approximately corresponds to $0 \leq t \leq 595$ ms in real time t . The time step in the computation is taken as $\Delta t = 0.002$ over $0 \leq t \leq 6$ and $\Delta t = 0.001$ over $6 < t \leq 9.4$, where the grid redistribution is started from $t = 3$, and it is performed up to the end of computation every four time steps. The interval of normalized time t roughly coincides with the time duration from the beginning to the end of the experiment in Fig. 4 in Ref. [9], and the profiles (a), (b), (c), (d), (e) and (f) in Fig. 1 correspond to the video images (c), (e), (g), (h), (i), and (j) in Fig. 4 in Ref. [9] respectively.

The single-valuedness of the interface shape breaks between (a) and (b) in Fig. 1, where the sheet strength of a core rapidly increases (see Fig. 7). The detailed profiles including the magnitude of the amplitudes in the fully nonlinear stage (b)–(f) in Fig. 1 are unchanged even though we take other initial values, i.e., the temporal evolution of an interface at the fully nonlinear stage depends only on the Atwood number A and the smoothing parameter δ .

The parameter δ plays a part in cutting higher order Fourier modes [42] and generally, the speed of the roll-up slows down and the breakdown of the computations occurs at later time for larger values δ . We show the effect of δ in Fig. 2. This tendency that the curve at a fixed time t has more turns for smaller δ is also found in Refs. [29,32]. We choose $\delta = 0.15$ in all regularized calculations except Fig. 2 for the reason that the value agrees well with the experiments by Jacobs *et al.* [9].

Profiles of interfaces with different Atwood numbers $A = 0$, $A = 0.5$, and $A = 0.8$ at $t = 7.2$ are shown in Fig. 3. The parameter α is taken as $\alpha = -0.05$ for $A = 0.5$ and $A = 0.8$. The results for $A = 0.5$ were unchanged even though we take $\alpha = -0.1$, however, the computations for $A = 0.8$ broke down at an earlier time when $\alpha = -0.1$. The time steps in the computations are taken as $\Delta t = 0.002$ over $0 \leq t \leq 5$ and $\Delta t = 0.001$ over $5 < t \leq 9.4$ for $A = 0$, while $\Delta t = 0.001$ over $0 \leq t \leq 6$ and $\Delta t = 0.0002$ over $6 < t \leq 7.2$ for both $A = 0.5$ and $A = 0.8$ in which the grid redistribution is performed every four and five time steps in the intervals $0 \leq t \leq 6$ and $6 < t \leq 7.2$, respectively. When $A = 0$, the bubble and spike velocities are the same in the magnitude and the clustering as stated in the Appendix does not occur in the computation. Therefore, the grid redistribution is not used for this Atwood number. Note that the time interval $0 \leq t \leq 7.2$ for $A = 0.5$ and $A = 0.8$ does not indicate identical duration in real time for the two At-

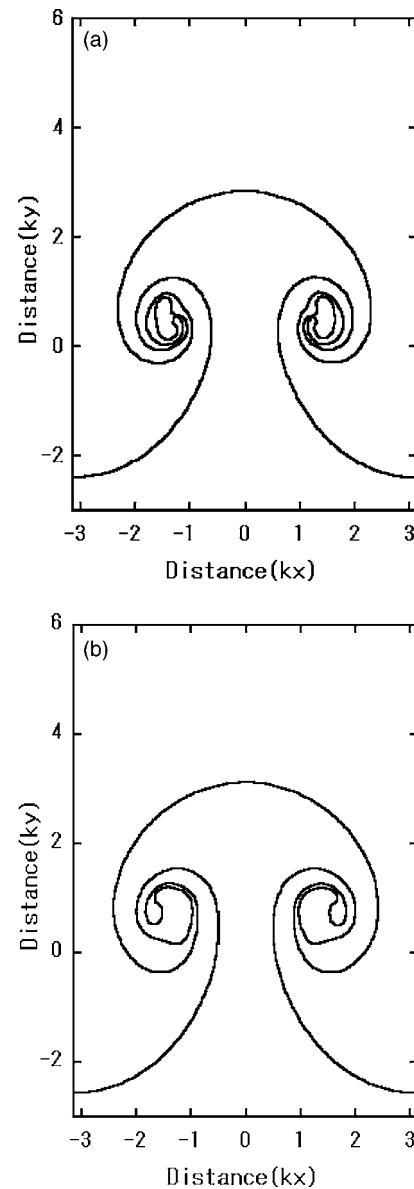


FIG. 2. Interfacial profiles in the RM instability at $t = 7.2$ with $\delta =$ (a) 0.1 and (b) 0.2, where $A = 0.155$ for both cases.

wood numbers, since the linear growth rate v_{lin} generally depends on the Atwood number. The velocity of a spike becomes larger and the roll-up becomes weaker as the Atwood number increases. The roll-up to the spiral is most tight at the Atwood number $A = 0$, while the roll-up is not seen for $A \geq 0.9$. This tendency is also observed in the RT instability [29,32].

The growth rates in different Atwood numbers are shown in Fig. 4. The bubble velocities gradually approach zero for all Atwood numbers, while spike velocities decay to some values which are determined by the Atwood numbers. As we see from the figure, the growth rate of a bubble is larger for lower Atwood numbers, while the growth rate of a spike is larger for higher Atwood numbers, which is also presented by the weakly nonlinear analysis [12]. This trend for the growth rate of a bubble differs from that in the RT instability, in which the growth rate of a bubble is larger for higher

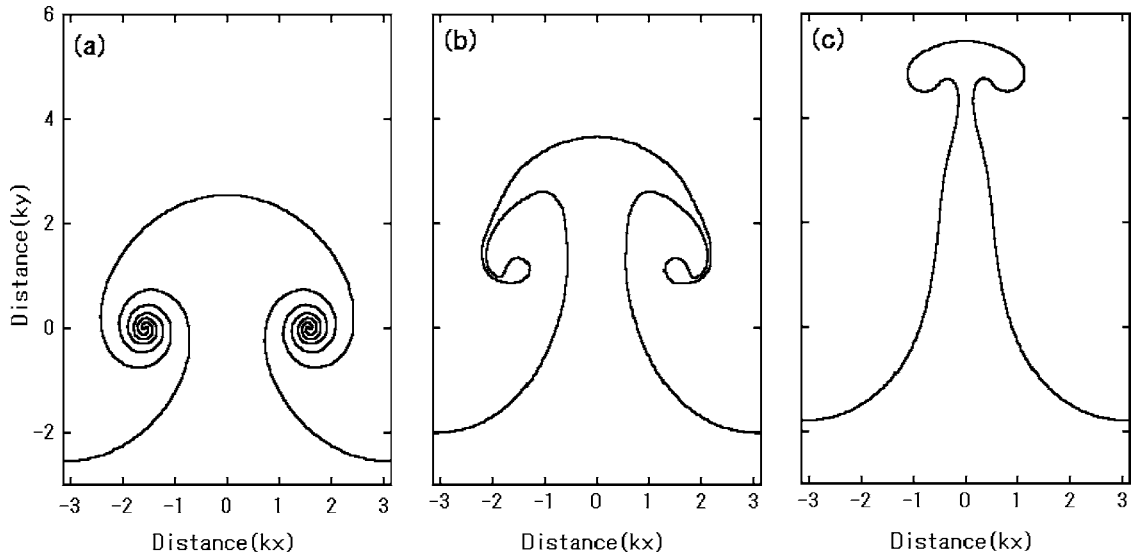


FIG. 3. Interfacial profiles in the RM instability for $A=$ (a) 0, (b) 0.5, and (c) 0.8 at $t=7.2$.

Atwood numbers [29,32] (see also Fig. 13 in Sec. V).

The strength of vortex sheets for various Atwood numbers is depicted in Fig. 5. Positions where the absolute value of the strength κ has a maximum value are located at spiral cores, which are centers of two counter-rotating spirals. These spiral cores may correspond to “vortex projectiles” (VPs) presented by Zabusky [43], which are coherent vortex structures of positive and negative circulation in two dimensions. Two peaks at around $\theta = \pm 1.5$ in Fig. 5(a) gradually approach each other as the Atwood number increases [$\theta = \pm 1.1$ in (b) and $\theta = \pm 0.4$ in (c)]. As the passage of time, opposite signed sheet strength and same signed secondary sheet strength with the core strength appear in the neighborhood of the cores. The appearance of these weak opposite signed and same signed secondary sheet strength which is not observed when $A=0$, is also confirmed by direct simulations of the Euler equation [12,44], in which the strength of a sheet corresponds to the vorticity induced on the interface. In Ref. [44] Peng *et al.* numerically solved the compressible Euler equation, in which they pointed out that opposite signed secondary vorticities arise due to baroclinic effect and the phenomenon is clearer for higher Atwood numbers as found in our simulations. These secondary vorticities are also observed in numerical simulations in Ref. [12]. A jump discontinuity which appears in the neighborhood of the spike at $A=0.8$ [Fig. 5(c)] is sharper as $A \rightarrow 1$. This jump discontinuity for higher Atwood numbers is also observed in the RT instability [29,32].

Figure 6 shows loci of the vortex cores that appear in $[-\pi, 0]$ for $A=0.155$, $A=0.5$, and $A=0.8$. Here, the position of a vortex core is defined as a point where the absolute value of the strength of a sheet κ takes a maximum value $\kappa = \kappa_m(\theta_m, t)$, where $\theta = \theta_m$ is a Lagrangian marker that provides the maximum value of κ , from which we see that a locus of the core is given by $(X(\theta_m, t), Y(\theta_m, t))$. The loci started from position $(-\pi/2, 0)$ at $t=0$ extend upward with (a) complicated and (c) monotonic motion for $A=0.155$ and $A=0.8$, respectively, while a slight zigzag is found at the late

stage in the core motion for $A=0.5$ (see the interfacial profiles in Figs. 1 and 3).

Temporal evolution of the strength of a vortex core κ_m , i.e., the maximum strength of a sheet in $-\pi \leq \theta \leq 0$ is shown in Fig. 7. When the Atwood number is relatively low, the

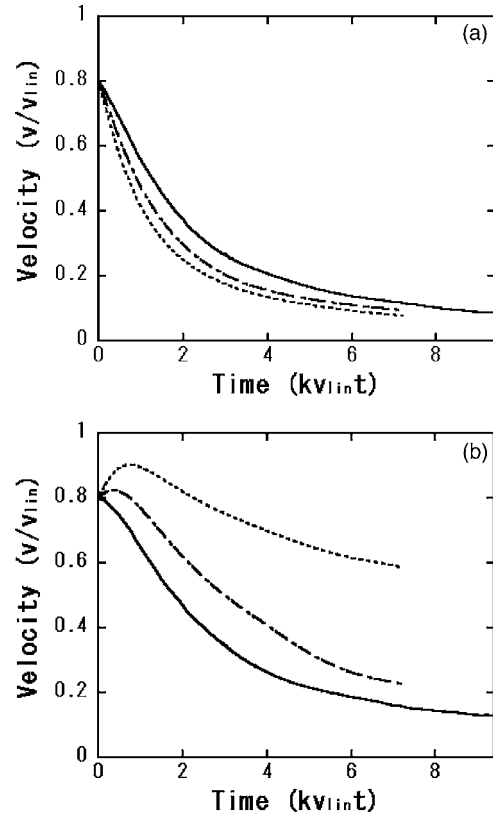


FIG. 4. Velocities of (a) bubbles and (b) spikes in the RM instability, where solid lines, dashed and dotted lines, and dashed lines depict $A=0.155$, $A=0.5$, and $A=0.8$, respectively and time intervals are taken as $0 \leq t \leq 9.4$ for $A=0.155$ and $0 \leq t \leq 7.2$ for both $A=0.5$ and $A=0.8$.

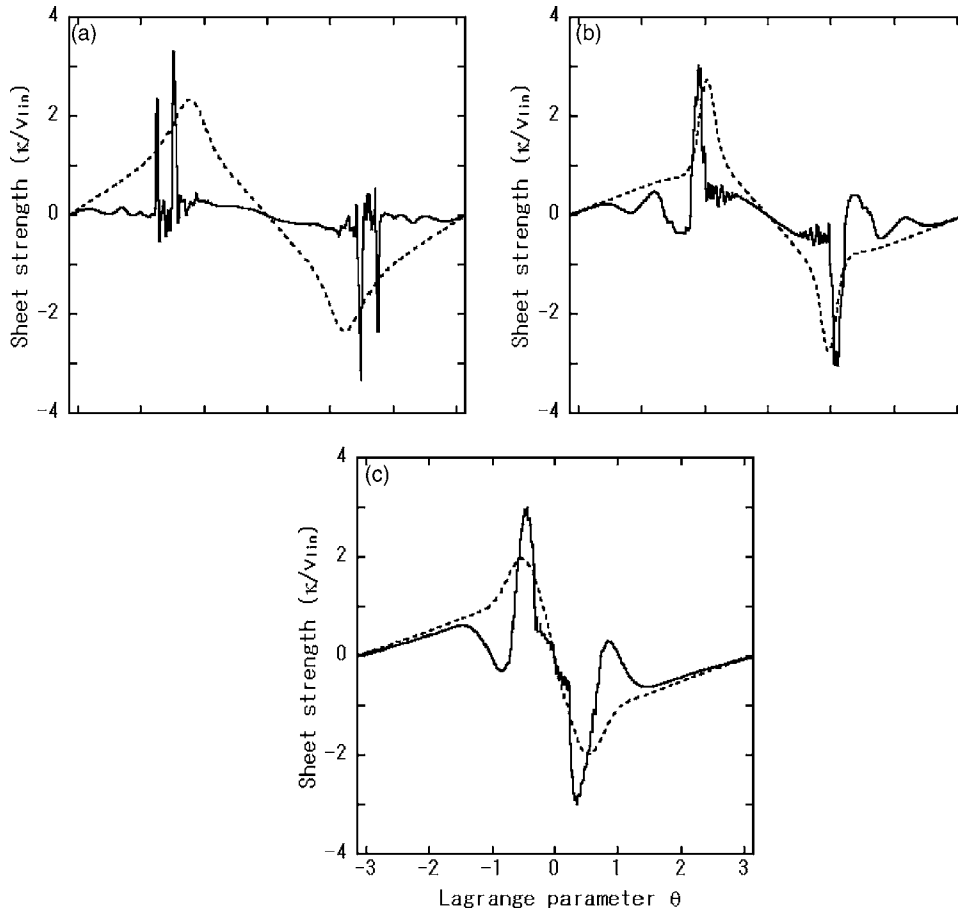


FIG. 5. Sheet strength κ for (a) $A=0.155$, (b) $A=0.5$, and (c) $A=0.8$, where dashed and solid lines in (a) depict $t=2.0$ and $t=8.6$, while dashed and solid lines in (b) and (c) both depict $t=2.8$ and $t=6.4$.

maximum strength κ_m repeats an increase and decrease with some oscillation in which the complicated motion of a core is reflected [see Fig. 6(a)]. This oscillation gradually disappears as the Atwood number increases and that is not found when $A \geq 0.8$ for which motion of a core is monotonous [see Fig. 6(b)]. As stated above, the strength of a core rapidly grows at the beginning of the roll-up ($2 < t < 3$ for $A=0$ and $A=0.155$, while $3 < t < 4$ for $A=0.5$), where the fully nonlinear stage begins. When $A=0$, the strength of a core increases with a regular oscillation that is connected with turns of a sheet. This increase of κ reflects the behavior of $1/s_\theta$ in $\kappa = \Gamma_\theta/s_\theta$, because Γ_θ is a constant when $A=0$. As we see from the figure, the absolute values of the strength of a core in the RM instability are larger for lower Atwood numbers.

IV. SINGULARITY FORMATIONS IN RICHTMYER-MESHKOV INSTABILITY

In this section, we investigate singularity formations in the RM instability. Since the occurrence of singularity formations is predicted in the limit of the interface thickness zero, we set the regularized parameter $\delta=0$ in this section. We also set the parameter $\alpha=-A$ so that we can compare the theoretical work by Baker *et al.* for singularity formations in the RT instability (see Sec. V B). On calculations of the integral equation Eq. (6) including the Cauchy integral in Eq. (4), we use the alternate point quadrature method by Sidi and Israeli [22] stated in the Appendix. The grid redistribution is

not performed here. The time step is set to $\Delta t=2.0 \times 10^{-6}$ and $N=1024$ (the mode number $M=256$, see the Appendix) throughout this section, and initial configurations are given by Eq. (7).

For the KH instability, Moore [26] analytically examined the solution to the Birkhoff-Rott equation (3) as a function of the circulation Γ with initial condition,

$$Z(\Gamma, 0) = \Gamma + i\epsilon \sin \Gamma,$$

where $\epsilon \ll 1$ is the initial amplitude of the vortex sheet. Assuming that

$$Z(\Gamma, t) = \Gamma + 2i \sum_{m=1}^{\infty} A_m(t) \sin m\Gamma, \quad (8)$$

he obtained the asymptotic expression for A_m ,

$$|A_m| \sim C m^{-5/2} \exp \left[m \left(1 + \frac{1}{2}t + \frac{1}{4} \log \epsilon t \right) \right], \quad (9)$$

where C is a constant that is independent of mode number m . This power law for the amplitude of the Fourier coefficient is known as Moore's $-5/2$ power law. The analytic solution to the Birkhoff-Rott equation loses its analyticity at a finite time $t=t_c$, which satisfies the following relation:

$$1 + \frac{1}{2}t_c + \frac{1}{4} \log \epsilon t_c = 0.$$

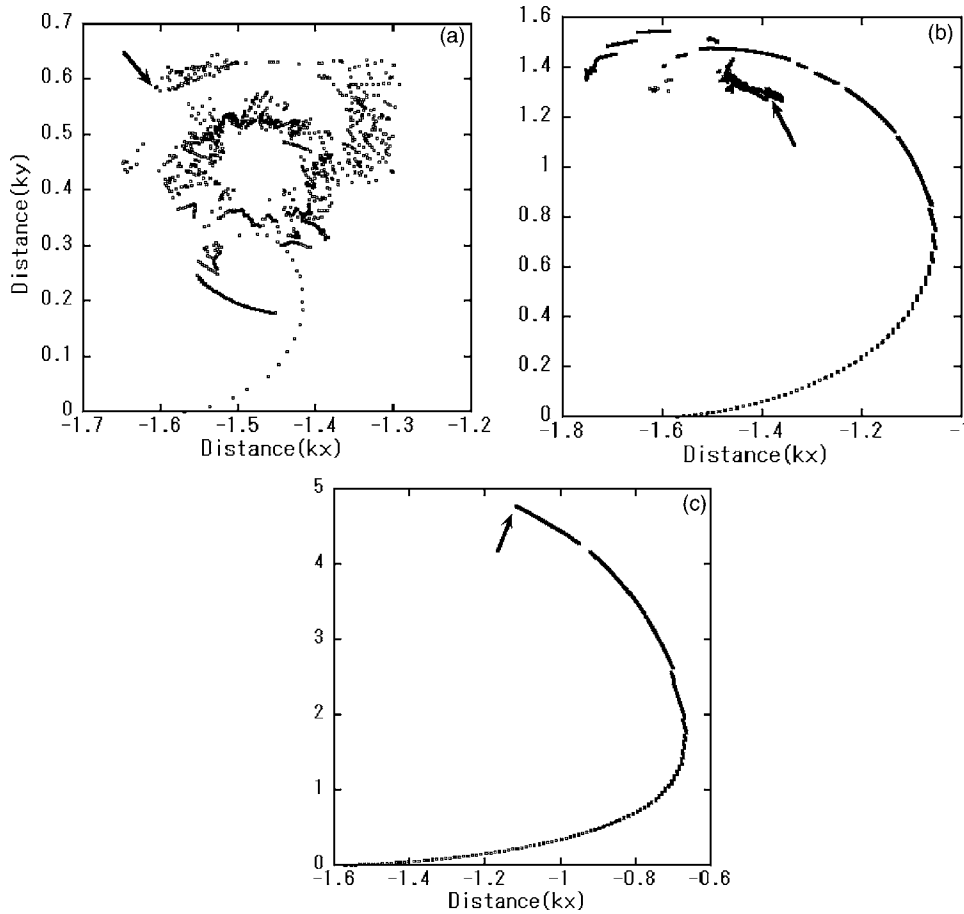


FIG. 6. Loci of a vortex core $(X(\theta_m, t), Y(\theta_m, t))$ in $-\pi \leq \theta \leq 0$ for (a) $A=0.155$ over $0 \leq t \leq 9.4$, (b) $A=0.5$ over $0 \leq t \leq 7.2$ and (c) $A=0.8$ over $0 \leq t \leq 7.2$, where all arrows point to final positions in the loci.

Then the curvature of the vortex sheet diverges as $|x - x_c|^{-1/2}$ in the neighborhood of the singular point $x = x_c$, since the parameter Γ is proportional to the coordinate x in the KH instability as found in the parametrization of the vortex sheet in Z [see Eq. (8)].

The strength of the vortex sheet κ has the form

$$\kappa(\Gamma, t) = 1 - \frac{\sqrt{3}}{t} \{t_c - t + [(t_c - t)^2 + 4\Gamma^2]^{1/2}\}^{1/2} + \mathcal{O}\left(\frac{1}{t_c}\right), \quad (10)$$

as $t \rightarrow t_c$, therefore, $\kappa(t_c)$ has a cuspidal form $|x - x_c|^{1/2}$. These analytical predictions for the KH instability are supported by several numerical works [39–41], however, it is unknown whether or not analogous singularity formations occur in the RM instability. In this section, we show that the singularity formations can also occur in the RM instability.

For the RM instability, we expand

$$Z(\theta, t) = \theta + \sum_{m=-\infty}^{\infty} \hat{C}_m(t) e^{im\theta}, \quad \kappa(\theta, t) = \sum_{m=-\infty}^{\infty} \hat{\kappa}_m(t) e^{im\theta},$$

and suppose that there exists some constant β such that the asymptotic form of the Fourier coefficient \hat{C}_m can be written as

$$|\hat{C}_m(t)| \propto m^{-\beta} e^{f(A, m, t)} \quad (t \gg 1), \quad (11)$$

where $f(A, m, t)$ is a function of the Atwood number A , mode number m , and time t . We define critical time t_c in the RM instability as a time when $f(A, m, t_c) = 0$ in Eq. (11). Then the second derivative of Z with respect to the Lagrangian variable θ , which determines the curvature of a vortex sheet, diverges for some β such that $2 - \beta < 0$. Note that the critical

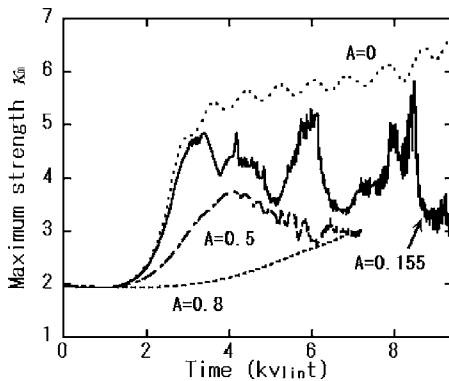


FIG. 7. Temporal evolutions of core strength κ_m in the RM instability, where dotted, solid, dashed, and dotted-dashed lines depict $A=0$, $A=0.155$, $A=0.5$, and $A=0.8$, respectively, in which time intervals are taken that $0 \leq t \leq 9.4$ for $A=0$ and $A=0.155$, while $0 \leq t \leq 7.2$ for $A=0.5$ and $A=0.8$. As the secondary vorticity becomes larger ($A=0.155$) and ($A=0.5$), the maximum strength κ_m turns to decrease [see also Fig. 5 and Fig. 14].

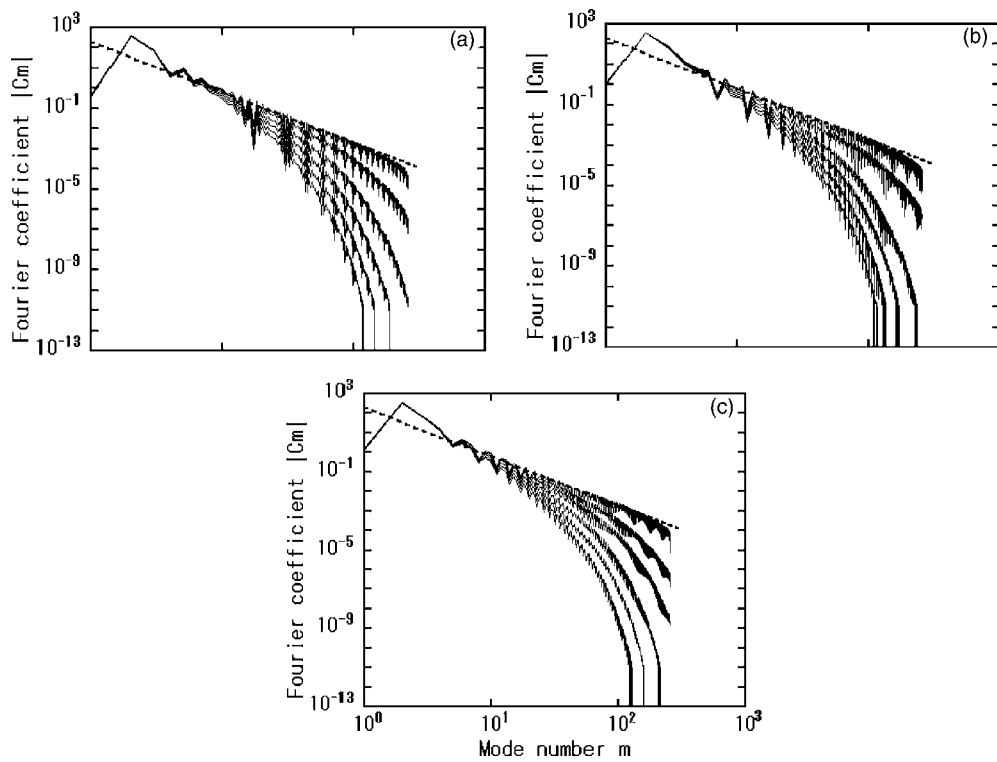


FIG. 8. Log-log plots of the Fourier coefficients for (a) $A=0.155$ at time $t=4.00 \times 10^{-3}, 4.10 \times 10^{-3}, 4.20 \times 10^{-3}, 4.30 \times 10^{-3}, 4.40 \times 10^{-3}, 4.49 \times 10^{-3}$, (b) $A=0.5$ at $t=3.70 \times 10^{-3}, 3.80 \times 10^{-3}, 3.90 \times 10^{-3}, 4.00 \times 10^{-3}, 4.14 \times 10^{-3}, 4.20 \times 10^{-3}$, and (c) $A=1.0$ at $t=3.20 \times 10^{-3}, 3.30 \times 10^{-3}, 3.40 \times 10^{-3}, 3.50 \times 10^{-3}, 3.56 \times 10^{-3}, 3.62 \times 10^{-3}$. The slope of the dashed line is $-5/2$, the value obtained by Moore for the KH instability.

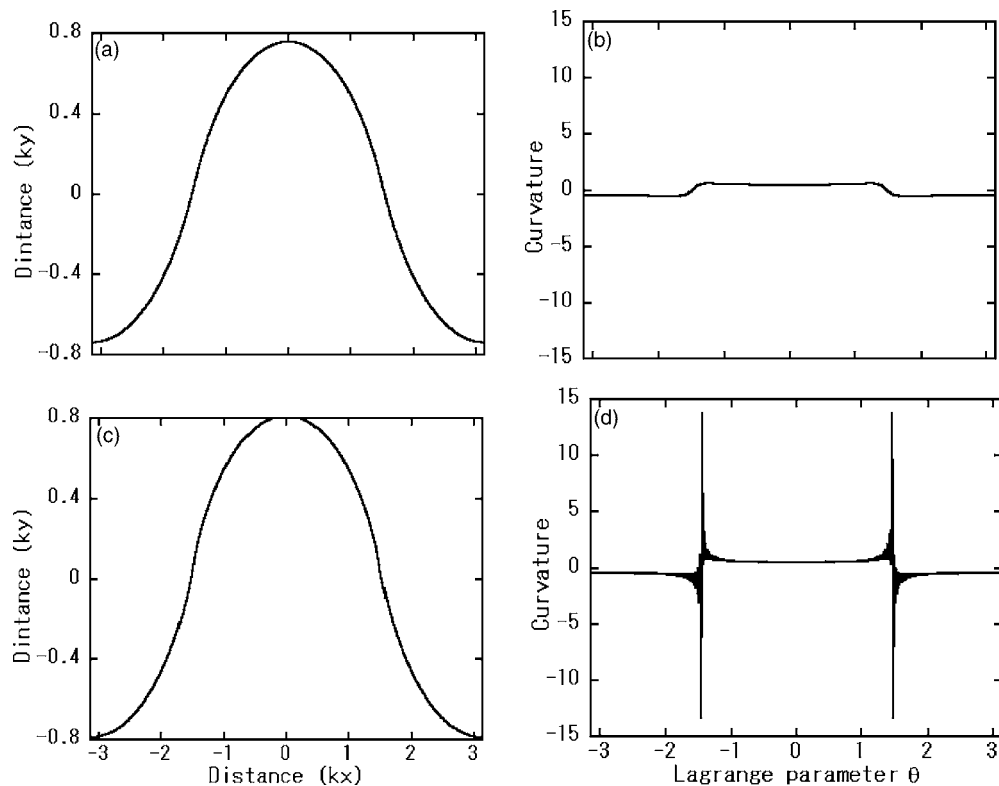


FIG. 9. Interfacial profiles and the curvatures for $A=0.155$ at $t=4.40 \times 10^{-3}$ [(a) and (b)] and $t=4.49 \times 10^{-3}$ [(c) and (d)].

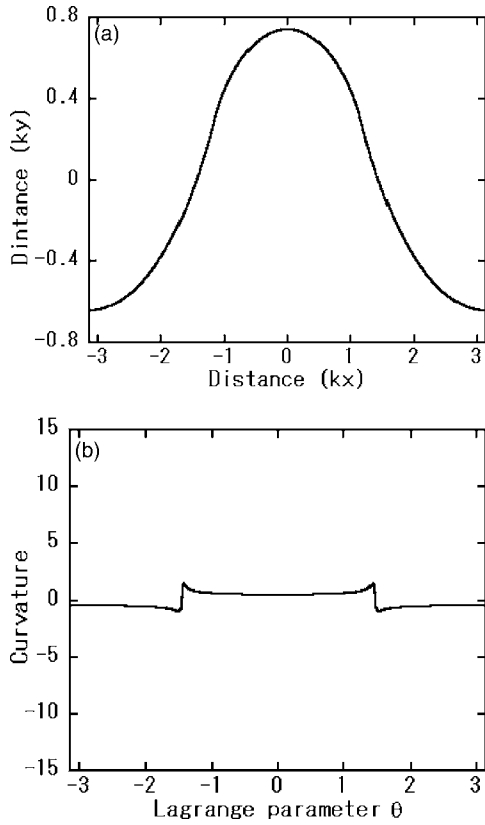


FIG. 10. Interfacial profile and the curvature for $A=1$ at $t=3.62 \times 10^{-3}$.

time t_c generally depends on the Atwood number A for the RM instability. Under these assumptions, we detect the exponent β numerically.

Figure 8 shows amplitudes of the Fourier coefficients $|\hat{C}_m(t)|$ versus mode number, where dashed lines in the figure have slope $-5/2$, i.e., the value predicted by Moore for the KH instability. The spectra approach to $-5/2$ lines as time t approaches the critical time t_c , where $t_c=4.49 \times 10^{-3}$, $t_c=4.20 \times 10^{-3}$, and $t_c=3.62 \times 10^{-3}$ for $A=0.155$, $A=0.5$, and for $A=1.0$, respectively.

Interfacial profiles and curvatures for $A=0.155$ at $t=4.40 \times 10^{-3}$ and $t=4.49 \times 10^{-3}$ are shown in Fig. 9. The interfacial profile at (c) $t=4.49 \times 10^{-3}$ is smooth; however, two discontinuities in the neighborhood of $\pm\pi/2$ appear in the curvature profile. After a few time steps of this critical time, the curvature of the vortex sheet diverges and the computations break down. The counterpart for $A=1.0$ at $t=3.62 \times 10^{-3}$ is shown in Fig. 10. Sharp discontinuities as found in Fig. 9(d) are not observed in the curvature profile for this Atwood number; in spite of that, the Fourier coefficient fits the $-5/2$ line [see Fig. 8(c)]. Generally, the height of discontinuities in curvature profiles is lower for higher Atwood numbers.

In Fig. 11 we show the sheet strength κ for several times, where the solid lines (a) and (b) depict the critical sheet strength $\kappa(\theta, t_c)$ for the Atwood numbers. We see that the sheet strength forms two cusps at critical time $t_c=4.49 \times 10^{-3}$ and $t_c=3.62 \times 10^{-3}$ for $A=0.155$ and $A=1.0$, respectively. The existence of cusps in κ suggests that the sheet

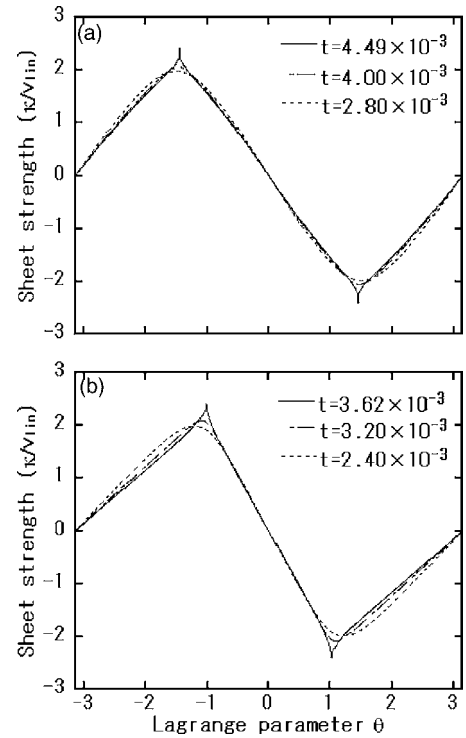


FIG. 11. Sheet strength κ in the RM instability at $\delta=0$ for $A=(a)$ 0.155 and (b) 1.0, the dashed, dashed-dotted, and solid lines depict $t=2.80 \times 10^{-3}$, $t=4.00 \times 10^{-3}$, and $t=4.49 \times 10^{-3}$ in (a), while they depict $t=2.40 \times 10^{-3}$, $t=3.20 \times 10^{-3}$, and $t=3.62 \times 10^{-3}$ in (b), respectively.

strength has the form of $\kappa \sim |\theta|^{\beta'}$ in the neighborhood of cusp points for some $\beta' < 1$ as $t \rightarrow t_c$, as analogous to the KH instability case.

When one singularity is formed at the critical time, the other physical quantities should also have some singularities. On the contrary, if a physical quantity does not have singular form at the critical time t_c , neither have the other quantities. It seems that the curvature profile for $A=1$ suggests that the singularity formations do not occur at this Atwood number, even though the Fourier spectrum fits the $-5/2$ line and the sheet strength has cuspidal form at the time.

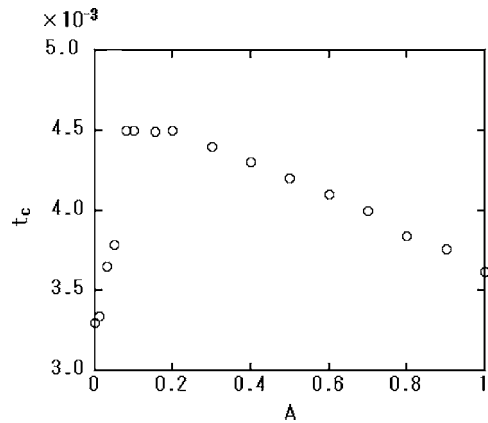


FIG. 12. Critical time t_c in the RM instability for various Atwood numbers.

Dependence of the critical time t_c on various Atwood numbers is depicted in Fig. 12. The critical time t_c increases from $A=1$ to approximately $A=0.08$ and it rapidly decreases with the decrease of the Atwood number for $A < 0.08$, especially for $0 \leq A < 0.05$. The dependence of critical time t_c on Atwood numbers in the RM instability is considerably different from that in the RT instability, which will be stated in the next section (see Fig. 18).

V. CORE STRENGTH AND SINGULARITY FORMATIONS IN RAYLEIGH-TAYLOR INSTABILITY

In this section we present corresponding results to Secs. III and IV for the RT instability for the purpose of comparison with the RM instability. Detailed discussions for interfacial profiles and the growth rate of a bubble and spike in the RT instability are found in Refs. [29,32]; therefore, we only briefly describe that here. In order to investigate the RT instability, we add the gravity term to the Bernoulli equation (2),

$$\frac{d\Gamma}{dt} = -2A \frac{d\Phi}{dt} + A\mathbf{q} \cdot \mathbf{q} - \frac{A-2\alpha}{4} \boldsymbol{\kappa} \cdot \boldsymbol{\kappa} + \alpha A \boldsymbol{\kappa} \cdot \mathbf{q} - 2Ag_y,$$

which leads to

$$\begin{aligned} \kappa_t = & -\frac{2A}{s_\theta} (X_\theta U_t + Y_\theta V_t) - \frac{(1-\alpha A)\kappa}{s_\theta^2} (X_\theta U_\theta + Y_\theta V_\theta) \\ & - \frac{A-\alpha}{4s_\theta} (\kappa^2)_\theta - 2Ag \frac{y_\theta}{s_\theta}, \end{aligned} \quad (12)$$

instead of Eq. (6), where g is the gravitational acceleration. By solving Eq. (4) coupled with Eq. (12), we can determine motion of a vortex sheet in the RT instability.

We normalize the gravitational acceleration $g \rightarrow g/(kv_{\text{lin}}^2)$ so that it becomes dimensionless. The initial configurations of the interfacial profile $Z(\theta, 0)$ and the vorticity $\kappa(\theta, 0)$ in the RT instability are given as

$$Z(\theta, 0) = \theta + ia_0 \cos \theta, \quad \kappa(\theta, 0) = 0, \quad (13)$$

where the normalized gravitational acceleration $g = -1$ throughout this section, in which the minus sign implies that gravity acts vertically upwards, i.e., the fluid in the upper side across the interface is lighter than the lower one.

A. Vortex core strength in Rayleigh-Taylor instability

In Fig. 13, profiles of an interface with different Atwood numbers $A=0.5$ and $A=0.8$ are shown. The time step Δt is taken that $\Delta t=0.001$ over $0 \leq t \leq 5$ for both Atwood numbers, while $\Delta t=0.0002$ over $5 < t \leq 7$ and $5 < t \leq 6$ for $A=0.5$ and $A=0.8$, respectively, where the grid redistribution is performed every four and five time steps for the intervals $0 \leq t \leq 5$ and $5 < t \leq 7(6)$ at $A=0.5$ (0.8), respectively. The profiles are similar to those for the RM instability in Fig. 3 for each Atwood number. Generally, final profiles in the computation in the RT instability are very similar to those in the RM instability at the same Atwood numbers in spite of the difference of their growth rates.

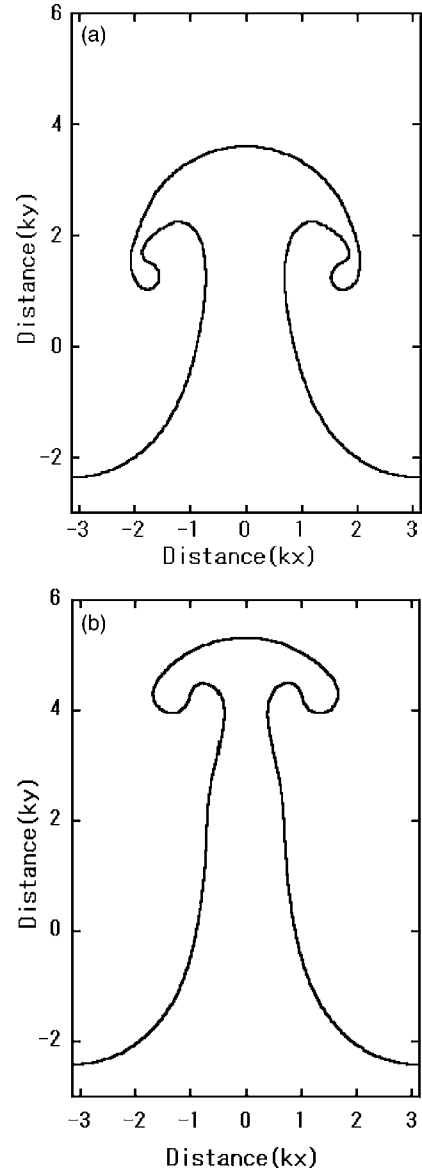


FIG. 13. Profiles of an interface in the RT instability for (a) $A=0.5$ at $t=7$ and (b) $A=0.8$ at $t=6$.

Temporal evolution of the maximum strength, i.e., the sheet strength of a vortex core in $-\pi \leq \theta \leq 0$ is shown in Fig. 14. The properties that the maximum strength κ_m irregularly oscillates for relatively low Atwood numbers and the oscillation gradually disappears as the Atwood number increases are also preserved for the RT instability, however, the absolute values of the core strength are larger for higher Atwood numbers, contrary to the RM instability (see Fig. 7). This tendency suggests that the tightness of the roll-up does not necessarily indicate that the sheet strength of a core region is large. Note that the absolute values of core strength in the RT instability finally become larger than the counterparts in the RM instability for relatively higher Atwood numbers, in spite of the fact that the initial sheet strength $\kappa(\theta, 0) = 0$ in the RT instability (see $A=0.5$ and $A=0.8$ lines in Figs. 7 and 14).

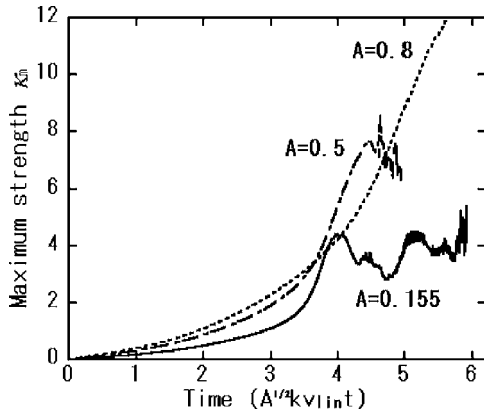


FIG. 14. Temporal evolutions of core strength κ_m in the RT instability, where solid, dashed-dotted, and dashed lines depict $A=0.155$, $A=0.5$, and $A=0.8$, respectively.

B. Singularity formations in Rayleigh-Taylor instability

For the RT instability, there are some theoretical predictions for singularity formations as stated in Sec. I [28,34]. Baker *et al.* [28] extended the Lagrangian parameter θ to a complex valued variable and examined the analyticities of solutions Z and κ to Eqs. (3) and (12) for $\alpha=-A$, in which they obtained the result that the curvature singularity can occur at a finite time $t=t_c$ for $A \neq 1$. For $A=1$, they predict that the singularity will not appear in finite time. Tanveer [34] also investigated the singularity formation in the RT instability for $A=1$ by using the conformal mapping and concluded that singularities are formed in the unphysical plane; however, it cannot reach the physical plane in finite time.

In this section we examine the singularity formations in the RT instability numerically and compare to the theoretical predictions stated above, and at the same time, we clarify the difference between the singularity formations in the RM instability. We set that all numerical parameters and numerical methods including the tolerance level in the iteration are the same as those for calculations of singularity formations for the RM instability performed in Sec. IV excluding the time step. The time step is taken that $\Delta t=1.0 \times 10^{-4}$ throughout this section. Initial configurations are given by Eq. (13).

In Fig. 15 we show amplitudes of the Fourier coefficients $|\hat{C}_m(t)|$ versus mode number m , where dashed lines in (a) and (b) in the figure have slope $-5/2$. The spectra approach to the $-5/2$ lines as time t approaches critical time $t_c=0.4640$ for $A=0.155$ and $t_c=0.1684$ for $A=1.0$, where critical time t_c is defined in a similar manner as Eq. (11) in Sec. IV. The Fourier spectra in the RT instability also fit to Moore's $-5/2$ power law for various Atwood numbers, which is also predicted by Baker *et al.* for $A < 1$ [28].

Interfacial profiles and curvatures at $t_c=0.4640$ for $A=0.155$ and $t_c=0.1684$ for $A=1.0$ are shown in Fig. 16. The discontinuities in the curvature profile (d) for $A=1.0$ are much weaker than those in (b) for $A=0.155$. Analogous to the RM instability case, the height of discontinuities in curvature profiles for the RT instability is also lower for higher Atwood numbers. The vague discontinuities in the curvature profile for $A=1.0$ may suggest that the singularity formation

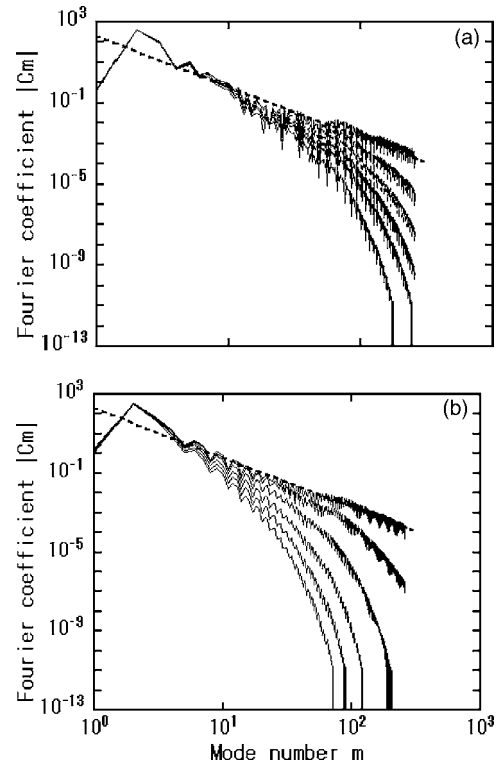


FIG. 15. Log-log plots of Fourier coefficients for $A=(a) 0.155$ and (b) 1.0, where plotted time is $t=0.4520, 0.4560, 0.4580, 0.4600, 0.4620,$ and 0.4640 in (a) and $0.1520, 0.1560, 0.1600, 0.1640, 0.1670,$ and 0.1684 in (b), respectively. The dashed line in the figure has slope $-5/2$.

does not occur in finite time for this Atwood number, as predicted by Baker *et al.* [28] and Tanveer [34].

Figure 17 shows the sheet strength κ up to critical time t_c , where solid lines (a) and (b) depict the critical sheet strength $\kappa(\theta, t_c)$ for the Atwood number. Unlike the RM instability case (see Fig. 11), the amplitude of the cuspidal form for the RT instability is larger for higher Atwood numbers. This may be related to the fact that the strength of a vortex core for $\delta \neq 0$ is larger for higher Atwood numbers (see Fig. 14).

Dependence of the critical time t_c on the Atwood numbers is depicted in Fig. 18, where the dashed line and squares denote the theoretical prediction by Baker *et al.* [28] and our numerical computations, respectively. When $A \neq 0$, the critical time t_c in the RT instability is estimated by Baker *et al.* [28] as

$$t_c = \frac{\tilde{C}}{|Ag|^{1/2}}, \tag{14}$$

where the constant \tilde{C} generally depends upon the initial conditions in the computation. Our numerical computations support this theoretical result, although it is unclear whether the curvature singularity occurs or not for $A > 0.9$ as found in Fig. 16(d). Both Baker *et al.* [28] and Tanveer [34] predict that some singularity exists in the complex, i.e., unphysical plane, however, it will never reach the real axis, i.e., physical

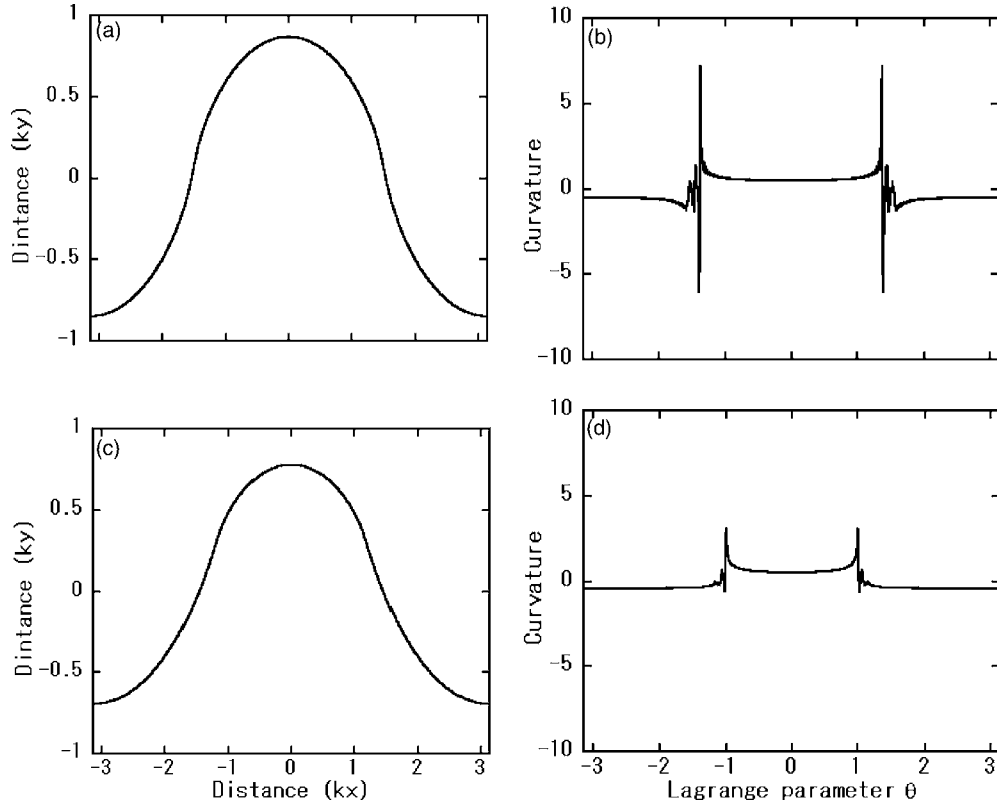


FIG. 16. Interfacial profiles and curvatures at $t=0.4640$ for $A=0.155$ [(a) and (b)] and at $t=0.1684$ for $A=1.0$ [(c) and (d)], where (b) and (d) are curvature profiles of the interfacial profiles (a) and (c), respectively.

plane. It is not easy to verify this prediction for $A=1$ by numerical computations as pointed out in Ref. [28].

VI. DISCUSSIONS AND CONCLUSION

We have investigated the behavior of a vortex core and the singularity formations in the RM instability with the Birkhoff-Rott equation coupled with the evolution equation for the sheet strength. When the Atwood number is finite, the numerical computations in order to examine the roll-ups become unstable, especially for higher Atwood numbers, due to the clustering of grid points. In case that we do not perform the rearrangement of grid points such that they are placed equidistantly, the breakdown of computations is caused at relatively early stage of the roll-ups even though $A=0.155$ in both the RM and RT instabilities.

The trajectory of a vortex core in the RT instability is similar to the one found in Fig. 6 for the RM instability for the corresponding Atwood number including the range over which the vortex core moves. From this result, including the interfacial profiles and the behavior of the maximum sheet strength found in Figs. 7 and 14, we can see that both instabilities have similar properties as vortex sheets, at least when $\delta \neq 0$.

For the singularity formations, we have numerically confirmed that the Fourier amplitude \hat{C}_m for $Z_m = X_m + iY_m$ obeys Moore's $-5/2$ power law for various Atwood numbers over $0 \leq A \leq 1$ for both RM and RT instabilities, although the results for higher Atwood numbers, especially for $A > 0.9$, may

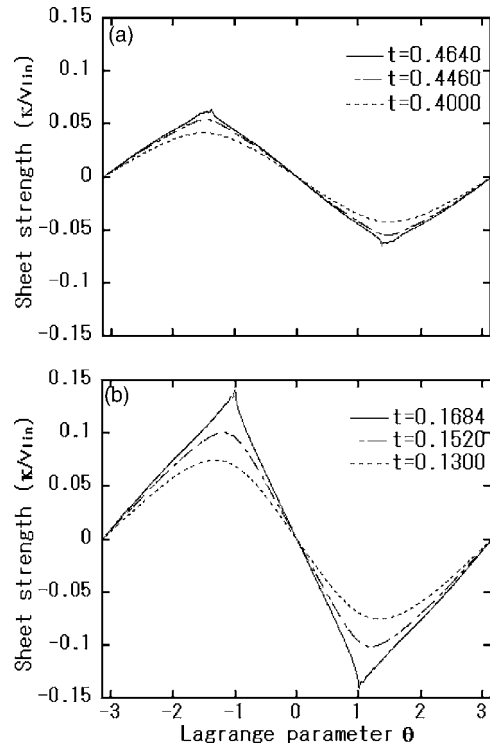


FIG. 17. Sheet strength κ in the RT instability at $\delta=0$ for $A=(a)$ 0.155 and (b) 1.0, the solid, dashed-dotted, and dashed lines depict $t=0.4640, 0.4460,$ and 0.4000 in (a), while $t=0.1684, 0.1520,$ and 0.1300 in (b), respectively.

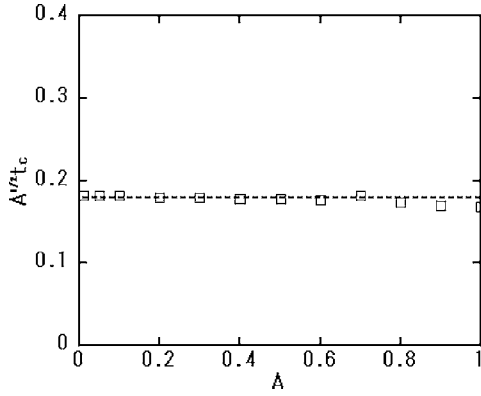


FIG. 18. Critical time $\sqrt{A}t_c$ in the RT instability for various Atwood numbers, where squares denote our numerical calculations, while the dashed line gives the theoretical prediction by Baker *et al.*

not necessarily lead to the formation of the curvature singularity. For the RM instability, this is the first work that has shown that the Fourier spectra of the amplitude of the interface fit Moore's $-5/2$ power law.

The cuspidal formations in the sheet strength κ appear for all Atwood numbers including $A=1$ for both RM and RT instabilities, however, the curvature singularities are hardly observed for higher Atwood numbers, especially for $A \geq 0.9$ for both RM and RT instabilities. When the singularity formations occur, all physical quantities should be singular at that time. It seems that the vague discontinuities in the curvature profiles in Figs. 10(b) and 16(d) suggest that the singularity formations do not occur for $A=1$ for both RM and RT instabilities.

We have investigated singularity formations for $\alpha=-A$ in Secs. IV and V B, however, other choices for the parameter α are also possible. Since α is an artificial and nonphysical parameter, the generic nature of singularities should not depend on the choices of α . For several α , we confirmed this consideration numerically for both RM and RT instabilities, i.e., the critical time t_c for the Atwood number, the profiles of the curvature, and the sheet strength at the critical time are not affected by the choice of α .

As we see from Figs. 12 and 18, the most remarkable difference between the RM and RT instabilities for singularity formations is in the dependence of critical time t_c on the Atwood numbers. As for the RM instability, the theoretical estimate of t_c is an open problem that needs further investigation in the future.

ACKNOWLEDGMENTS

The authors thank Professor Y. Fukumoto and Professor J. G. Wouchuk for their fruitful discussions. The authors thank Professor T. Sakajo for useful comments and advice for computer simulations.

APPENDIX

In this appendix we present numerical methods in order to solve the governing equations, Eqs. (4) and (6). Discretized equations to Eq. (5) are given as

$$U_j = -\frac{h}{4\pi} \sum_{\substack{cm=0 \\ cm \neq j}}^{N-1} \frac{\sinh(Y_j - Y_m) \kappa_m s_{\theta,m}}{\cosh(Y_j - Y_m) - \cos(X_j - X_m) + \delta^2},$$

$$V_j = \frac{h}{4\pi} \sum_{\substack{cm=0 \\ cm \neq j}}^{N-1} \frac{\sin(X_j - X_m) \kappa_m s_{\theta,m}}{\cosh(Y_j - Y_m) - \cos(X_j - X_m) + \delta^2}, \quad (\text{A1})$$

in which $X_j \equiv X(\theta_j)$, $Y_j \equiv Y(\theta_j)$, and $\kappa_j \equiv \kappa(\theta_j)$ are expanded into discrete Fourier series

$$X_j = \theta_j + \sum_{m=-M}^M \hat{X}_m e^{im\theta_j}, \quad Y_j = \sum_{m=-M}^M \hat{Y}_m e^{im\theta_j},$$

$$\kappa_j = \sum_{m=-M}^M \hat{\kappa}_m e^{im\theta_j} \quad (j=0, \dots, N-1), \quad (\text{A2})$$

with the derivatives

$$X_{\theta,m} = 1 + \sum_{m=-M}^M im \hat{X}_m e^{im\theta_j},$$

$$Y_{\theta,m} = \sum_{m=-M}^M im \hat{Y}_m e^{im\theta_j},$$

$$\kappa_{\theta,m} = \sum_{m=-M}^M im \hat{\kappa}_m e^{im\theta_j}, \quad (\text{A3})$$

where $X_{\theta,m} = (\partial X / \partial \theta)_m$ and so on. Note that the derivatives (A3) do not involve errors which necessarily arise in derivative representations by usual difference approximations.

When we perform numerical computations, we take the number of grid points N in $\theta_j = 2\pi j/N$ ($j=0, \dots, N-1$) with $\theta_N = 2\pi$ as at least $N=4M+1$ for the mode number M and make a zero-padded zone in order to remove the aliasing by convolutions that occur from nonlinear terms in Eqs. (4) and (6), i.e., we set

$$\hat{X}_m = 0, \quad \hat{Y}_m = 0, \quad \hat{\kappa}_m = 0 \quad (m=M+1, \dots, N/2).$$

How many zero values are needed in removing of the aliasing is usually determined from the highest order of nonlinear terms in equations as found in the estimate of "3/2 rule," i.e., $N \geq 3M+1$ for the Burgers equation in spectral methods or the collocation method [45]. Here, the order cannot be determined clearly because of the existence of the term s_θ in denominators in Eqs. (4) and (6). However, the contribution to higher order frequency components due to this term is small compared to those of numerators, especially the one from the last term $(\kappa^2)_\theta$ on the right-hand side of Eq. (6), which causes a shocklike structure as found in the solution of the Burgers equation. In our computations, the cutoff was incomplete for the grid number N such that $N \leq 3M+1$. Taking these into account, we take $N=4M+1$ as the value of the least cutoff frequency here.

As pointed out by Kerr [29] and Sohn [32], point vortices, i.e., the grid points on the interface, tend to make a cluster

around a bubble when the Atwood number is high, which is caused by the fact that the velocity difference between a bubble and spike becomes large for higher Atwood numbers. As a result of that, grid points around a spike decrease and the calculation fails due to numerical instabilities. In order to avoid that, we use a grid redistribution method developed by Baker *et al.* [25,46] so that grid points are arranged equidistantly. This method is analogous to the node spreading presented by Kerr so as to obtain equally located grid points [29], however, the accuracy in the grid redistribution method is higher than his method and we can take more grid points. The grid redistribution method is as follows. Now we have a representation for the interface $(X(\theta, t), Y(\theta, t))$ with equally spaced Lagrangian markers θ at a time t . Then we seek a new mapping from $[0, 2\pi]$ onto itself, $\theta \rightarrow p$, such that

$$p = \frac{1}{L} \int_0^\theta s_\theta(\theta') d\theta', \quad (\text{A4})$$

in which $s_\theta = \sqrt{X_\theta^2 + Y_\theta^2}$ and L is the whole length of the interface at the time t ,

$$L = \frac{1}{2\pi} \int_0^{2\pi} s_\theta(\theta') d\theta'. \quad (\text{A5})$$

Since we want to evenly space grid points $p = mh$ ($m = 0, \dots, N$), where $h = 2\pi/N$, N , the number of grid points, we seek the following sequence:

$$mh = \frac{1}{L} \int_0^{\bar{\theta}_m} s_\theta(\theta') d\theta' \quad (m = 0, \dots, N). \quad (\text{A6})$$

Note that $\bar{\theta}_m$ ($m = 0, \dots, N$) with $\bar{\theta}_0 = \theta_0$ and $\bar{\theta}_N = \theta_N$ in Eq. (A6) mapped to mh in p is not equally divided $\theta_m = 2\pi m/N$ but a new position in θ which is not necessarily evenly spaced. In order to find these new parametrizations successively, Newton's method is used. Integrals in Eqs. (A4) and (A5) are evaluated by the Fourier series of the integrand.

Once new marker $\bar{\theta}_m$ is given, evenly spaced new position $(X(\bar{\theta}_m, t), Y(\bar{\theta}_m, t))$ and the strength $\kappa(\bar{\theta}_m, t)$ are determined by cubic splines using θ_m , $\bar{\theta}_m$ ($X(\theta_m, t), Y(\theta_m, t)$), and $\kappa(\theta_m, t)$. Thus, the redistribution of grid points at a time t is completed. With these new dependent variables, new velocities $X_t(\bar{\theta}_m, t)$, $Y_t(\bar{\theta}_m, t)$, and $\kappa_t(\bar{\theta}_m, t)$ are evaluated at time t , then we can regard the discrete variable θ_j in the Fourier series $X_j - \bar{\theta}_j$, Y_j , κ_j as the ones in the mapped space p , where the points are distributed with equal interval h . This redistribution is performed every few time steps when we calculate the roll-up of the interface in Secs. III and V A.

For the calculation of the Cauchy integral in Eqs. (4) and (6), we adopt the trapezoidal rule when $\delta \neq 0$, while the alternate point quadrature method by Sidi and Israeli [22] is used for calculations of $\delta = 0$. In this quadrature method, the discretizations of Eq. (5) are given as follows:

$$U_j = -\frac{2h}{4\pi} \sum_{\substack{m=0 \\ j+m:\text{odd}}}^{N-1} \frac{\sinh(Y_j - Y_m) \kappa_m s_{\theta,m}}{\cosh(Y_j - Y_m) - \cos(X_j - X_m)},$$

$$V_j = \frac{2h}{4\pi} \sum_{\substack{m=0 \\ j+m:\text{odd}}}^{N-1} \frac{\sin(X_j - X_m) \kappa_m s_{\theta,m}}{\cosh(Y_j - Y_m) - \cos(X_j - X_m)}, \quad (\text{A7})$$

where the summation is taken from nearest points to far points in the order in opposite sides of a singular point $j = m$. This quadrature method has been adopted for computations for singularity formations in a vortex sheet in the KH instability [39,40]. Here, we use this method in order to solve the Fredholm integral equation Eq. (6) in addition to the calculation of the Cauchy integral in Eq. (3) when we examine singularity formations in RM and RT instabilities in Secs. IV and V B. We add that when we use this quadrature method, the iteration must be performed so as not to change the order of rows and columns in the matrix which appears in the integral equation.

-
- [1] R. D. Richtmyer, *Commun. Pure Appl. Math.* **13**, 297 (1960).
[2] E. E. Meshkov, *Fluid Dyn.* **4**, 101 (1969).
[3] Y. Yang, Q. Zang, and D. H. Sharp, *Phys. Fluids* **6**, 1856 (1994).
[4] G. Dimonte, C. E. Frerking, M. Schneider, and B. Remington, *Phys. Plasmas* **3**, 614 (1996).
[5] A. L. Velikovich, *Phys. Fluids* **8**, 1666 (1996).
[6] J. G. Wouchuk and K. Nishihara, *Phys. Plasmas* **3**, 3761 (1996); **4**, 1028 (1997).
[7] J. G. Wouchuk, *Phys. Plasmas* **8**, 2890 (2001); *Phys. Rev. E* **63**, 056303 (2001).
[8] A. L. Velikovich, J. P. Dahlburg, A. J. Schmitt, J. H. Gardner, L. Phillips, F. L. Cochran, Y. K. Chong, G. Dimonte, and N. Metzler, *Phys. Plasmas* **7**, 1662 (2000).
[9] J. W. Jacobs and J. M. Sheeley, *Phys. Fluids* **8**, 405 (1996).
[10] K. Nishihara and G. Wouchuk, *Osaka Univ. ILE Ann. Prog. Rep.* **2002**, 249 (2002).
[11] Q. Zhang and S. Sohn, *Phys. Fluids* **9**, 1106 (1997).
[12] C. Matsuoka, K. Nishihara, and Y. Fukuda, *Phys. Rev. E* **67**, 036301 (2003).
[13] D. Layzer, *Astrophys. J.* **122**, 1 (1955).
[14] S. I. Abarzhi, *Phys. Fluids* **12**, 3112 (2000).
[15] S. I. Abarzhi, *Phys. Fluids* **13**, 2866 (2001).
[16] S. I. Abarzhi, *Phys. Lett. A* **294**, 95 (2002).
[17] S. I. Abarzhi, K. Nishihara, and J. Glimm, *Phys. Lett. A* **317**, 470 (2003).
[18] G. Birkhoff, *Proceedings of the Symposium on Applied Mathematics XIII* (American Mathematical Society, Providence, RI, 1962), p. 55.
[19] N. Rott, *J. Fluid Mech.* **1**, 111 (1956).
[20] P. G. Saffman, *Vortex Dynamics* (Cambridge University Press, Cambridge, 1992), p. 141, and references therein.
[21] G. R. Baker, D. I. Meiron, and S. A. Orszag, *J. Fluid Mech.* **123**, 477 (1982).

- [22] A. Sidi and M. Israeli, *J. Sci. Comput.* **3**, 201 (1988).
- [23] R. Krasny, *J. Fluid Mech.* **184**, 123 (1987).
- [24] R. Caflisch and O. Orellana, *SIAM J. Math. Anal.* **20**, 293 (1989).
- [25] G. R. Baker and M. J. Shelley, *J. Fluid Mech.* **215**, 161 (1990).
- [26] D. W. Moore, *Proc. R. Soc. London, Ser. A* **365**, 105 (1979).
- [27] R. Caflisch, O. Orellana, and M. Siegel, *SIAM J. Appl. Math.* **50**, 1517 (1990).
- [28] G. Baker, R. Caflisch, and M. Siegel, *J. Fluid Mech.* **252**, 51 (1993).
- [29] R. M. Kerr, *J. Comput. Phys.* **76**, 48 (1988).
- [30] A. D. Kotelnikov, J. Ray, and N. J. Zabusky, *Phys. Fluids* **12**, 3245 (2000).
- [31] C. E. Niederhaus and J. W. Jacobs, *Proceedings of the Fourth Microgravity Fluid Physics* (Cleveland, Ohio, 1998), p. 528.
- [32] S. I. Sohn, *Phys. Rev. E* **69**, 036703 (2004).
- [33] D. I. Pullin, *J. Fluid Mech.* **119**, 507 (1982).
- [34] S. Tanveer, *Proc. R. Soc. London, Ser. A* **441**, 501 (1993).
- [35] R. E. Caflisch and J. Lowengrub, *SIAM (Soc. Ind. Appl. Math.) J. Numer. Anal.* **26**, 1060 (1989).
- [36] C. Bögers, *Math. Comput.* **53**, 141 (1989).
- [37] J. S. Ely and G. R. Baker, *J. Comput. Phys.* **111**, 275 (1993).
- [38] J. W. Rottman and P. K. Stanby, *J. Fluid Mech.* **247**, 527 (1993).
- [39] M. J. Shelley, *J. Fluid Mech.* **244**, 493 (1992).
- [40] T. Sakajyo, *Phys. Fluids* **14**, 2886 (2002).
- [41] R. Krasny, *J. Fluid Mech.* **167**, 65 (1986).
- [42] O. Friedrich and T. Sonar, *Math. Methods Appl. Sci.* **18**, 615 (1995).
- [43] N. Zabusky, *Annu. Rev. Fluid Mech.* **31**, 495 (1999).
- [44] G. Peng, N. Zabusky, and S. Zhang, *Phys. Fluids* **15**, 3730 (2003).
- [45] R. Peylet, *Spectral Methods for Incompressible Viscous Flow* (Springer, New York, 2002), Sec. 2.9.
- [46] G. Baker and A. Nachbin, *SIAM J. Sci. Comput. (USA)* **19**, 1737 (1998).